Resonant mixing of optical orbital and spin angular momentum by using chiral silicon nanosphere clusters

Ahmed Al-Jarro, Claudiu G. Biris, and Nicolae C. Panoiu*

Department of Electronic and Electrical Engineering, University College London, Torrington Place, London WC1E 7JE, United Kingdom

**n.panoiu@ucl.ac.uk*

Abstract: We present an in-depth analysis of the resonant intermixing between optical orbital and spin angular momentum of Laguerre-Gaussian (LG) beams, mediated by chiral clusters made of silicon nanospheres. In particular, we establish a relationship between the spin and orbital quantum numbers characterizing the LG beam and the order q of the rotation symmetry group $\mathscr{C}_q$ of the cluster of nanospheres for which resonantly enhanced coupling between the two components of the optical angular momentum is observed. Thus, similar to the case of diffraction grating-mediated transfer of linear momentum between optical beams, we demonstrate that clusters of nanospheres that are invariant to specific rotation transformations can efficiently transfer optical angular momentum between LG beams with different quantum numbers. We also discuss the conditions in which the resonant interaction between LG beams and a chiral cluster of nanospheres leads to the generation of superchiral light.

References and links

1. V. S. Liberman and B. Y. Zeldovich, "Spin-orbit interaction of a photon in an inhomogeneous medium," Phys. Rev. A **46**, 5199–5207 (1992).
2. O. Hosten and P. Kwiat, "Observation of the spin Hall effect of light via weak measurements," Science **319**, 787–790 (2008).
3. G. Nienhuis, "Angular Momentum and Vortices in Optics," in *Structured Light and Its Applications: An Introduction to Phase-Structured Beams and Nanoscale Optical Forces*, ed. D. L. Andrews (Elsevier, New York, 2008, pp. 19).
4. K. Y. Bliokh, A. Aiello, and M. A. Alonso, "Spin-orbit interactions of light in isotropic media," in *The Angular Momentum of Light*, eds. D. L. Andrews and M. Babiker (Cambridge University, 2012, pp. 174).
5. R. Y. Chiao and Y. S. Wu, "Manifestations of Berrys topological phase for the photon," Phys. Rev. Lett. **57**, 933–936 (1986).
6. A. Tomita and R. Y. Chiao, "Observation of Berrys topological phase by use of an optical fiber," Phys. Rev. Lett. **57**, 937–940 (1986).
7. M. Onoda, S. Murakami, and N. Nagaosa, "Hall effect of light," Phys. Rev. Lett. **93**, 083901 (2004).
8. K. Y. Bliokh, "Geometrodynamics of polarized light: Berry phase and spin Hall effect in a gradient-index medium," J. Opt. A **11**, 094009 (2009).
9. G. Biener, A. Niv, V. Kleiner, and E. Hasman, "Formation of helical beams by use of Pancharatnam-Berry phase optical elements," Opt. Lett. **27**, 1875–1877 (2002).
10. L. Marrucci, C. Manzo, and D. Paparo, "Optical spin-to-orbital angular momentum conversion in inhomogeneous anisotropic media," Phys. Rev. Lett. **96**, 163905 (2006).

11. Y. Gorodetski, A. Drezet, C. Genet, and T. W. Ebbesen, "Generating Far-Field Orbital Angular Momenta from Near-Field Optical Chirality," Phys. Rev. Lett. **110**, 203906 (2013).
12. E. Brasselet, G. Gervinskas, G. Seniutinas, and S. Juodkazis, "Topological Shaping of Light by Closed-Path Nanoslits," Phys. Rev. Lett. **111**, 193901 (2013).
13. G. Li, M. Kang, S. Chen, S. Zhang, E. Y. Pun, K. W. Cheah, and J. Li, "Spin-enabled plasmonic metasurfaces for manipulating orbital angular momentum of light," Nano Lett. **13**, 4148–4151 (2013).
14. D. Lin, P. Fan, E. Hasman, and M. L. Brongersma, "Dielectric gradient metasurface optical elements," Science **345**, 298–302 (2014).
15. Y. Zhao, J. S. Edgar, G. D. M. Jeffries, D. McGloin, and D. T. Chiu, "Spin-to-orbital angular momentum conversion in a strongly focused optical beam," Phys. Rev. Lett. **99**, 073901 (2007).
16. H. Adachi, S. Akahoshi, and K. Miyakawa, "Orbital motion of spherical microparticles trapped in diffraction patterns of circularly polarized light," Phys. Rev. A **75**, 063409 (2007).
17. Y. Zhao, D. Shapiro, D. McGloin, D. T. Chiu, and S. Marchesini, "Direct observation of the transfer of orbital angular momentum to metal particles from a focused circularly polarized Gaussian beam," Opt. Express **17**, 23316–23322 (2009).
18. Y. Gorodetski, K. Y. Bliokh, B. Stein, C. Genet, N. Shitrit, V. Kleiner, E. Hasman, and T. W. Ebbesen, "Weak Measurements of Light Chirality with a Plasmonic Slit," Phys. Rev. Lett. **109**, 013901 (2012).
19. D. Haefner, S. Sukhov, and A. Dogariu, "Spin Hall effect of light in spherical geometry," Phys. Rev. Lett. **102**, 123903 (2009).
20. N. Shitrit, I. Yulevich, E. Maguid, D. Ozeri, D. Veksler, V. Kleiner, and E. Hasman, "Spin-optical metamaterial route to spin-controlled photonics," Science **340**, 724–726 (2013).
21. X. Cai, J. Wang, M. J. Strain, B. Johnson-Morris, J. Zhu, M. Sorel, J. L. OBrien, M. G. Thompson, S. Yu, "Integrated Compact Optical Vortex Beam Emitters," Science **338**, 363–366 (2012).
22. X. Wang, J. Chen, Y. Li, J. Ding, C. Guo, and H. Wang, "Optical orbital angular momentum from the curl of polarization," Phys. Rev. Lett. **105**, 253602 (2010).
23. L. Allen, M. W. Beijersbergen, R. J. C. Spreeuw, and J. P. Woerdman, "Orbital angular momentum of light and the transformation of Laguerre–Gaussian laser modes," Phys. Rev. A **45**, 8185–8189 (1992).
24. N. Heckenberg, R. McDuff, C. Smith, and A. White, "Generation Of Optical-Phase Singularities By Computer-Generated Holograms," Opt. Lett. **17**, 221–223 (1992).
25. M. W. Beijersbergen, L. Allen, H. Vanderveen, and J. P. Woerdman, "Astigmatic laser mode converters and transfer of orbital angular momentum," Opt. Commun. **96**, 123–132 (1993).
26. V. Kotlyar, A. Almazov, S. Khonina, V. Soifer, H. Elfstrom, and J. Turunen, "Generation of phase singularity through diffracting a plane or Gaussian beam by a spiral phase plate," J. Opt. Soc. Am. A **22**, 849–861 (2005).
27. A. S. Rury and R. Freeling, "Mie scattering of purely azimuthal Laguerre-Gauss beams: Angular-momentum-induced transparency," Phys. Rev. A **86**, 053830 (2012).
28. B. Tatian, "Fitting refractive-index data with the Sellmeier dispersion formula," Appl. Opt. **23**, 4477–4485 (1984).
29. M. Mishchenko, L. Travis, and A. Laci, *Scattering, Absorption and Emission of Light by Small Particles* (Cambridge University, Cambridge, 2002).
30. B. Stout, J. C. Auger, and J. Lafait, "A transfer matrix approach to local field calculations in multiple scattering problems," J. Mod. Opt. **49**, 2129–2152 (2002).
31. C. F. Bohren and D. R. Huffman, *Absorption and Scattering of Light by Small Particles* (Wiley, 1983).
32. D. A. Varshalovich, A. N. Moskalev, and V. K. Khersonskii, *Quantum Theory of Angular Momentum* (World Scientific, Singapore, 1988).
33. L. W. Davis, "Theory of electromagnetic beams," Phys. Rev. A **19**, 1177–1179 (1979).
34. G. Gouesbet, J. A. Lock, and G. Grehan, "Partial wave representations of laser beams for use in light scattering calculations," Appl. Opt. **34**, 2133–2143 (1995).
35. S. H. Simpson and S. Hanna, "Rotation of absorbing spheres in Laguerre–Gaussian beams," J. Opt. Soc. Am. A **26**, 173–183 (2009).
36. D. L. Andrews, *Structured Light and Its Applications: An Introduction to Phase-Structured Beams and Nanoscale Optical Forces* (Academic Press-Elsevier, Burlington, 2008).
37. D. Felbacq, G. Tayeb, and D. Maystre, "Scattering by a random set of parallel cylinders," J. Opt. Soc. Am. A **11**, 2526–2538 (1994).
38. E. Centeno and D. Felbacq, "Second-harmonic emission in two-dimensional photonic crystals," J. Opt. Soc. Am. B **23**, 2257–2264 (2006).
39. C. G. Biris and N. C. Panoiu, "Second harmonic generation in metamaterials based on homogeneous centrosymmetric nanowires," Phys. Rev. B **81**, 195102 (2010).
40. J. D. Jackson, *Classical Electrodynamics* (John Wiley, 3rd ed., 1998).
41. A. Garcia-Etxarri, R. Gomez-Medina, L. S. Froufe-Perez, C. Lopez, L. Chantada, F. Scheffold, J. Aizpurua, M. Nieto-Vesperinas, and J. J. Saenz, "Strong magnetic response of submicron silicon particles in the infrared," Opt. Express **19**, 4815–4826 (2011).
42. Y. Tang and A. E. Cohen, "Enhanced enantioselectivity in excitation of chiral molecules by superchiral light,"

Science **332**, 333–336 (2011).

43. Y. Tang and A. E. Cohen, "Optical chirality and its interaction with matter," Phys. Rev. Lett. **104**, 163901 (2010).

44. M. Schaferling, D. Dregely, M. Hentschel and H. Giessen, "Tailoring enhanced optical chirality: design principles for chiral plasmonic nanostructures," Pys. Rev. X **2**, 031010 (2012).

1. Introduction

Over the last decade, we have witnessed a tremendous growth of research interest in spin-orbit interactions (SOI) of light [1–4], both because of the implications of SOI related phenomena to our understanding of fundamental principles of optics and basic properties of light, as well as their potential technological applications to nanophotonics, microfluidics, optical microscopy, optical communications, and quantum information processing. Thus, generally optical beams carry two distinct types of angular momentum, namely spin angular momentum (SAM) linked to the polarization degrees of freedom of the electromagnetic field, and orbital angular momentum (OAM), which can be intrinsic or extrinsic, and is related to the spatial distribution of the field. When these two components are coupled via, e.g., light propagation in inhomogeneous optical media [5–8], interaction of optical beams with anisotropic structures or metasurfaces [9–14], and tight focusing of nonparaxial optical beams [15–17], a myriad of fascinating phenomena can occur, including spin-Hall effect of light, spin-to-orbital angular momentum conversion, and spin-dependent optical beam shaping [2, 7, 15, 18–22].

The research in the physics of SOI has been greatly facilitated by the availability of optical beams with well-defined angular momentum, which in the paraxial approximation can be naturally decomposed in an orbital and spin part. One such salient example is Laguerre–Gaussian, LG_{pl}, beams whose intensity profile in the transverse plane shows a concentric ring-like structure with $p + 1$ maxima and azimuthal phase dependence $e^{il\varphi}$, p and l being the radial and azimuthal indices, respectively. For such beams, in the paraxial case, the flux of the projection of the total angular momentum on the direction of propagation of the beam, J_z, is equal to $J_z = (l + \sigma)P/\omega$ [23], where P is the beam power, ω is the optical frequency, and $\sigma = \pm 1$ for circularly polarized light and $\sigma = 0$ for linearly polarized light. The widespread use of LG beams in studies of phenomena related to SOI is due to not only the particular properties of the angular momentum they carry but also the ease with which they can be produced in laboratory. In particular, approaches employing forked holograms, cylindrical lenses, and spiral phase plates [24–26] can be readily implemented in an experimental set-up.

A convenient approach to investigate SOI related phenomena is to analyze the scattering of optical beams from single or clusters of nanoparticles, primarily because the electromagnetic multipole modes of spherical nanoparticles possess well-defined values of the total angular momentum and its projection on a specific axis. For example, recently it has been demonstrated that the SOI can be resonantly enhanced when light is scattered from spherical particles [19] whereas this same interaction can be selectively suppressed in certain scattering channels when the incident light consists of LG beams [27]. The rotational symmetry of the scatterer can be broken by arranging nanoparticles in a cluster with q-fold rotational symmetry, case in which the conservation of angular momentum forbids the wave scattering in specific scattering channels when the incident beam has well-defined values of the angular momentum. Understanding the physics of these scattering processes is the main goal of this work. More specifically, in this article we provide a comprehensive description of the scattering of LG beams from clusters of spherical nanoparticles with specific rotational symmetry properties, by analyzing both the physical properties of the scattered far-field as well as the nature of the near-field.

The remaining of this article is organized as follows. In the next section we present the geometry and physical properties of the system of scatterers and the configuration of the optical wave excitation. Then, in Section 3, we outline the main features of the numerical method used

in our study. Section 4 contains the main results pertaining to light scattering by a single silicon nanosphere and chiral clusters made of such nanoparticles, whereas in Section 5, as a practical application of our analysis, we demonstrate that chiral clusters made of silicon nanospheres can be used to generate super-chiral light. Finally, in the last section, we summarize the main conclusions of our work.

2. Description of the optical beam scattering configuration

The configuration of the scattering of the LG optical beam from the cluster of nanoparticles is schematically presented in Fig. 1. Thus, we assume that a LG_{pl} optical beam propagating along the z-axis impinges on a cluster of spherical nanoparticles distributed in the (x,y)-plane. These nanoparticles are arranged in a chiral configuration with q-fold rotational symmetry. The axis of the LG beam passes through the center of the cluster and has minimum waist in the (x,y)-plane. To add specificity to our problem, we consider that the spherical nanoparticles are made of silicon, although the particular electromagnetic properties of the material only quantitatively affect the main conclusions of this work. Moreover, we chose the size of the spherical nanoparticles such that their resonances are located in the near- and mid-IR spectral range. Therefore, we neglected the intrinsic optical losses of silicon and assumed that the corresponding index of refraction is given by the Sellmeier equation [28].

In the general case, the incident electromagnetic field can be expressed as a multipole Fourier series expansion in the complete basis of vector spherical wave functions (VSWFs) [29,30], the so-called Mie series expansion [31]:

$$\mathbf{E}^{\text{inc}}(\mathbf{r}) = \sum_{mn} \left[a_{mn} \mathbf{M}_{mn}^{(1)}(k\mathbf{r}) + b_{mn} \mathbf{N}_{mn}^{(1)}(k\mathbf{r}) \right], \tag{1a}$$

$$\mathbf{H}^{\text{inc}}(\mathbf{r}) = -\frac{i}{\zeta} \sum_{mn} \left[b_{mn} \mathbf{M}_{mn}^{(1)}(k\mathbf{r}) + a_{mn} \mathbf{N}_{mn}^{(1)}(k\mathbf{r}) \right]. \tag{1b}$$

Here and in what follows we assume harmonic time dependence of the fields, $e^{-i\omega t}$, $\mathbf{r} = (r, \theta, \varphi)$ is the position vector, $\zeta = \sqrt{\mu/\varepsilon}$ is the impedance of the background medium, with μ and ε being the electric permittivity and magnetic permeability of the background, respectively, $\sum_{mn}(\cdot) = \sum_{n \geq 1} \sum_{m=-n}^{n} (\cdot)$, and $\mathbf{M}_{mn}^{(1)}$ and $\mathbf{N}_{mn}^{(1)}$ are the orthogonal VSWF [29–31] whose radial part is
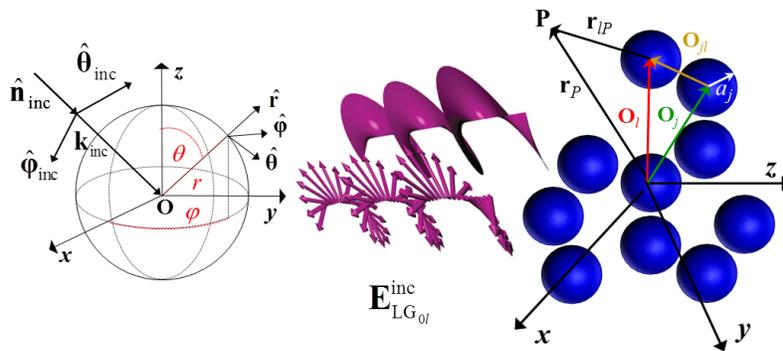

Fig. 1. Schematic of the system geometry and incident LG_{0l} beam. The optical beam propagates along the z-axis, the cluster of spherical nanoparticles is located in the (x,y)-plane, which coincide with the plane where the beam waist reaches its minimum value, and the center of the cluster is on the z-axis.

expressed in terms of spherical Bessel functions of the first kind and thus are finite at $r = 0$.

If the incident field is a plane wave (PW),

$$\mathbf{E}^{\text{inc}}(\mathbf{r}) = \mathbf{E}_0^{\text{inc}} e^{i\mathbf{k}_{\text{inc}} \cdot \mathbf{r}}, \tag{2}$$

the expansion coefficients are [29, 30]:

$$a_{mn}^{\text{PW}} = 4\pi i^n \mathbf{X}_{mn}^*(\hat{\mathbf{k}}_{\text{inc}}) \cdot \mathbf{E}_0^{\text{inc}}, \tag{3a}$$

$$b_{mn}^{\text{PW}} = 4\pi i^{n-1} \mathbf{Z}_{mn}^*(\hat{\mathbf{k}}_{\text{inc}}) \cdot \mathbf{E}_0^{\text{inc}}, \tag{3b}$$

where the asterisk denotes complex conjugate, $\hat{\mathbf{k}}_{\text{inc}}$ is a unit vector pointing along the direction of propagation of the incident PW, and $\mathbf{X}_{mn}$ and $\mathbf{Z}_{mn}$ are vector spherical functions given by:

$$\mathbf{X}_{mn}(\hat{\mathbf{r}}) = \left(\hat{\theta} \frac{im}{\sin\theta} d_{0m}^n(\theta) - \hat{\varphi} \frac{d}{d\theta} d_{0m}^n(\theta) \right) e^{im\varphi}, \tag{4a}$$

$$\mathbf{Z}_{mn}(\hat{\mathbf{r}}) = \left(\hat{\theta} \frac{d}{d\theta} d_{0m}^n(\theta) + \hat{\varphi} \frac{im}{\sin\theta} d_{0m}^n(\theta) \right) e^{im\varphi}. \tag{4b}$$

In these equations, $d_{0m}^n(\theta) = (-1)^{-m} \sqrt{(n-m)!/(n+m)!} P_n^m(\cos\theta)$ are the Wigner d-functions [32], with $P_n^m(\cos\theta)$ being the associated Legendre polynomials.

The coefficients in Eqs. (3) defining a PW can be used to construct LG beams. For simplicity, we consider in our study only LG$_{0l}$ beams as they possess all the properties we need to illustrate the main SOI related physics. Thus, the expansion coefficients defining LG$_{0l}$ beams, a_{mn}^{LG} and b_{mn}^{LG}, can be constructed from the PW coefficients in Eqs. (3) by using the following procedure. First, one introduces the fifth-order Davis shape coefficients, whose values depend only on n, defined as [33, 34]:

$$g_{1,n} = e^{-\alpha_n s^2}, \tag{5a}$$

$$g_{3,n} = g_{1,n} + \alpha_n s^4 (3 - \alpha_n s^2) e^{-\alpha_n s^2}, \tag{5b}$$

$$g_{5,n} = g_{3,n} + \alpha_n^2 s^8 \left(10 - 5\alpha_n s^2 + \frac{1}{2} \alpha_n^2 s^4 \right) e^{-\alpha_n s^2}, \tag{5c}$$

where $\alpha_n = (n-1)(n+2)$, $s = 1/(kw_0)$ defines the tightness of the focusing of the incident LG$_{0l}$ beam, $k = \omega/c$ being the wave number, $w_0 = \rho\lambda$ is the beam waist, with ρ a constant that determines the size of the beam waist.

We then introduce the column vector, $\mathbf{G}_{mn}^{\text{PW}} = g_{5,n} \left[a_{mn}^{\text{PW}}, b_{mn}^{\text{PW}} \right]^T$, where the symbol "$T$" means the transpose operation. Using these coefficients, we define the following expansion coefficients for LG beams that exhibit a phase variation of the form $e^{il\varphi}$ [35]:

$$\mathbf{C}_{mn}^{\text{LG}}(l,1) = \begin{cases} \mathbf{G}_{mn}^{\text{PW}}, & m = l+1 \\ 0, & \text{otherwise} \end{cases}, \quad \mathbf{C}_{mn}^{\text{LG}}(l,-1) = \begin{cases} \mathbf{G}_{mn}^{\text{PW}}, & m = l-1 \\ 0, & \text{otherwise} \end{cases}, \tag{6}$$

In our analysis we investigate LG$_{0l}$ beams that are propagating along the z axis, where the cluster of spherical nanoparticles is located in the (x, y)-plane. We also assume that the unit vectors $\hat{\theta}_{\text{inc}}$ and $\hat{\varphi}_{\text{inc}}$ that define the polarization of the incident field are oriented along the x- and y-axis, respectively. Under these conditions, the expansion coefficients $\mathbf{C}_{mn}^{\text{LG}}(l,-1)$, $\mathbf{C}_{mn}^{\text{LG},x}(l,0) = \frac{1}{\sqrt{2}} \left[\mathbf{C}_{mn}^{\text{LG}}(l,1) + \mathbf{C}_{mn}^{\text{LG}}(l,-1) \right]$, $\mathbf{C}_{mn}^{\text{LG},y}(l,0) = -\frac{i}{\sqrt{2}} \left[\mathbf{C}_{mn}^{\text{LG}}(l,1) - \mathbf{C}_{mn}^{\text{LG}}(l,-1) \right]$, and $\mathbf{C}_{mn}^{\text{LG}}(l,1)$ define LG$_{0l}$ beams that are circularly right polarized (CRP, $\sigma = -1$), linearly polarized (LP, $\sigma = 0$) along the x- or y-axis, and circularly left polarized (CLP, $\sigma = +1$), respectively. Note that the beam polarization is defined from the point of view of an observer who
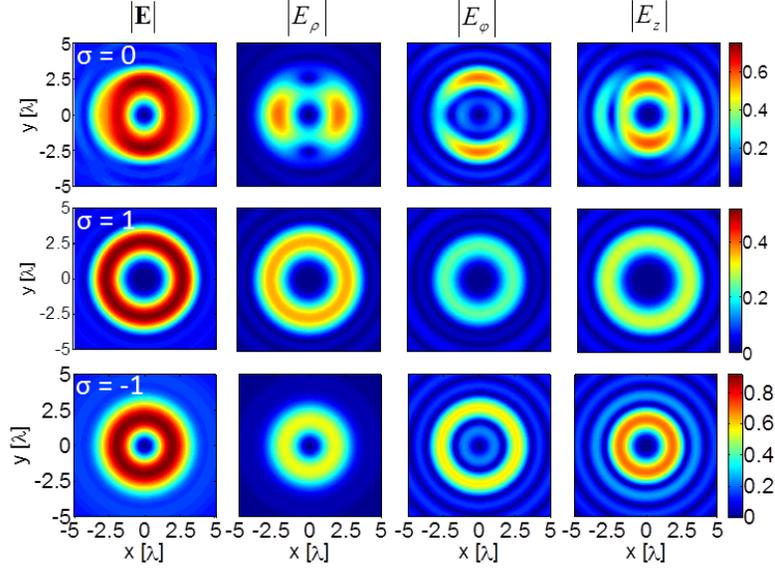
Fig. 2. Spatial distribution of the total electric field and its ρ-, φ-, and z-components, determined in the focal plane of a LG_{04} beam. Top, middle, and bottom panels correspond to $\sigma = 0$, $\sigma = 1$, and $\sigma = -1$, respectively, whereas the wavelength is $\lambda = 2515$ nm.

looks into the beam. These beams carry per photon an orbital and spin angular momentum equal to l and $\sigma = 0, \pm 1$, respectively, the total angular momentum being characterized by the integer, $j = l + \sigma$ [36].

In order to illustrate how this method can be used to construct LG beams, we show in Fig. 2 the electric field distribution for the LG_{04} beam, obtained by using Eq. (1a) and Eq. (6) with $n_{max} = 15$, $w_0 = 5\lambda$, and $\lambda = 2515$ nm. The top, middle, and bottom panels show the spatial distribution of the total electric field and its ρ-, φ-, and z-components (cylindrical coordinates projection), determined in the focal plane of a LG_{04} beam with $\sigma = 0$, $\sigma = 1$, and $\sigma = -1$, respectively. Note that all field components have comparable values and, as expected, the transverse size of the beam increases when the total angular momentum number, $j = l + \sigma$, increases.

3. Description of the numerical method

In this section we present the general framework of the multiple-scattering matrix (MSM) method [29, 31, 37–39], the approach on which our numerical simulations are based. To this end, let us go back to the system geometry presented in Fig. 1 and consider a cluster of N non-overlapping silicon spherical particles located in a dielectric background with electric permittivity, ε, and magnetic permeability, μ (for the sake of simplicity the background medium is here assumed to be vacuum, so that $\varepsilon = \varepsilon_0$ and $\mu = \mu_0$). The origin of the coordinate system, **O**, is set to coincide with the center of the cluster, defined by using some suitable "center of mass" relation. Moreover, to each particle, j, $j = 1, \ldots, N$, we associate a coordinate system with the origin at $\mathbf{O}_j = x_j \hat{\mathbf{x}} + y_j \hat{\mathbf{y}} + z_j \hat{\mathbf{z}}$, where $(\hat{\mathbf{x}}, \hat{\mathbf{y}}, \hat{\mathbf{z}})$ are the unit vectors along the axes of the Cartesian coordinate with the origin in **O**. The locations of the silicon spheres, assumed to have the same radius, $a = 500$ nm, are defined by the spherical coordinates of their centers, $\mathbf{O}_j$, that is $(r_j, \theta_j, \varphi_j)$, $j = 1, \ldots, N$, in the coordinate system with the origin in **O**. Furthermore, the position of the center of the lth particle, specified in a coordinate system with the origin in $\mathbf{O}_j$ is defined by the spherical coordinates, $(r_{jl}, \theta_{jl}, \varphi_{jl})$, whereas the position of an arbitrary point,

$\mathscr{P}$, defined with respect to the coordinate systems with the origin in $\mathbf{O}$ and $\mathbf{O}_j$ is specified by the spherical coordinates $\mathbf{r}_P = (r_P, \theta_P, \varphi_P)$ and $\mathbf{r}_{jP} = (r_{jP}, \theta_{jP}, \varphi_{jP})$, $j = 1, \dots, N$, respectively.

As shown in Fig. 1, the wavevector of the incident plane wave, $\mathbf{k}_{\text{inc}} = k\hat{\mathbf{n}}_{\text{inc}}$, is specified in the spherical coordinate system with origin in $\mathbf{O}$, with the unit vector $\hat{\mathbf{n}}_{\text{inc}}$ described by the angles θ_{inc} and φ_{inc}. Moreover, if we define the unit vectors, $\hat{\theta}_{\text{inc}}$ and $\hat{\varphi}_{\text{inc}}$, such that $\hat{\mathbf{n}}_{\text{inc}} = \hat{\theta}_{\text{inc}} \times \hat{\varphi}_{\text{inc}}$, the amplitude of the incident field in Eq. (2) can be expressed as $\mathbf{E}_0^{\text{inc}} = \mathbf{E}_\theta^{\text{inc}}\hat{\theta}_{\text{inc}} + \mathbf{E}_\varphi^{\text{inc}}\hat{\varphi}_{\text{inc}}$, where $\mathbf{E}_\theta^{\text{inc}}$ and $\mathbf{E}_\varphi^{\text{inc}}$ are the corresponding field components.

The first step of the MSM method is to perform a so-called Mie series expansion in VSWFs [29–31], as per Eq. (1) with $\mathbf{r} = \mathbf{r}_P$, of the incident electromagnetic field. This series expansion is performed in the coordinate system with the origin in $\mathbf{O}$ and thus is valid for all spheres. In the next step of our method we expand the fields scattered by each particle in series analogous to those given by Eq. (1a) and Eq. (1b), the difference being that for the scattered fields we employ the orthogonal VSWFs, $\mathbf{M}_{mn}^{(3)}$ and $\mathbf{N}_{mn}^{(3)}$, written in the coordinate system with origin in $\mathbf{O}_j$ and whose radial part is expressed in terms of outgoing spherical Hankel functions [29–31]. Thus, the fields scattered from the particle j, $j = 1, \dots, N$, is written as:

$$\mathbf{E}_j^{\text{sca}}(\mathbf{r}_{jP}) = \sum_{mn} \left[p_{mn}^j \mathbf{M}_{mn}^{(3)}(k\mathbf{r}_{jP}) + q_{mn}^j \mathbf{N}_{mn}^{(3)}(k\mathbf{r}_{jP}) \right], \quad r_{jP} > a, \tag{7a}$$

$$\mathbf{H}_j^{\text{sca}}(\mathbf{r}_{jP}) = -\frac{i}{\zeta} \sum_{mn} \left[q_{mn}^j \mathbf{M}_{mn}^{(3)}(k\mathbf{r}_{jP}) + p_{mn}^j \mathbf{N}_{mn}^{(3)}(k\mathbf{r}_{jP}) \right], \quad r_{jP} > a. \tag{7b}$$

where (p_{mn}^j, q_{mn}^j) are the expansion coefficients of the scattered field and represent the main unknowns of the scattering problem. Once (p_{mn}^j, q_{mn}^j) are calculated, the total field $\mathbf{F}^{\text{tot}}$, $\mathbf{F}^{\text{tot}} = \{\mathbf{E}^{\text{tot}}, \mathbf{H}^{\text{tot}}\}$, at $\mathbf{r}_P$ can be determined from:

$$\mathbf{F}^{\text{tot}}(\mathbf{r}_P) = \mathbf{F}^{\text{inc}}(\mathbf{r}_P) + \sum_{j=1}^{N} \mathbf{F}^{\text{sca}}(\mathbf{r}_{jP}). \tag{8}$$

Similarly, the fields inside the jth particle, $j = 1, \dots, N$, are expanded as:

$$\mathbf{E}_j^{\text{int}}(\mathbf{r}_{jP}) = \sum_{mn} \left[c_{mn}^j \mathbf{M}_{mn}^{(1)}(k\mathbf{r}_{jP}) + d_{mn}^j \mathbf{N}_{mn}^{(1)}(k\mathbf{r}_{jP}) \right], \quad r_{jP} < a, \tag{9a}$$

$$\mathbf{H}_j^{\text{int}}(\mathbf{r}_{jP}) = -\frac{i}{\zeta} \sum_{mn} \left[d_{mn}^j \mathbf{M}_{mn}^{(1)}(k\mathbf{r}_{jP}) + c_{mn}^j \mathbf{N}_{mn}^{(1)}(k\mathbf{r}_{jP}) \right], \quad r_{jP} < a. \tag{9b}$$

where (c_{mn}^j, d_{mn}^j) are the expansion coefficients of the internal field.

The relationships between the incident, scattered, and internal expansion coefficients can be conveniently expressed via a matrix associated to the system of scatterers, a method formally known as the T-matrix method [29, 30]. For this purpose, we introduce the following column vectors, $\mathbf{a}^j = [a_{mn}^j]^T$, $n \geq 1$, $m = -n, \dots, n$, and similarly for $\mathbf{b}^j$, $\mathbf{p}^j$, $\mathbf{q}^j$, $\mathbf{c}^j$, and $\mathbf{d}^j$. Therefore, assuming that the system contains only the jth particle, the relations among the expansion coefficients can be represented in a compact matrix form as, $[\mathbf{p}^j, \mathbf{q}^j]^T = \mathbf{T}_{\text{sca}}^j [\mathbf{a}^j, \mathbf{b}^j]^T$ and $[\mathbf{c}^j, \mathbf{d}^j]^T = \mathbf{T}_{\text{int}}^j [\mathbf{a}^j, \mathbf{b}^j]^T$, where $\mathbf{T}_{\text{sca}}^j$ and $\mathbf{T}_{\text{int}}^j$ are the scattering and internal matrices associated to the jth particle, respectively. Since in this study we consider systems containing only spherical particles, the matrices $\mathbf{T}_{\text{sca}}^j$ and $\mathbf{T}_{\text{int}}^j$ are diagonal matrices.

For the jth scatterer in the N-particle system, the incoming field can be viewed as the linear superposition of the incident optical field and the sum of the fields that are scattered by all the other particles. Therefore, the coefficients of the scattered field, $[\mathbf{p}^j, \mathbf{q}^j]^T$, obey the following

matrix equation:

$$\begin{bmatrix} \mathbf{p}^j \\ \mathbf{q}^j \end{bmatrix} = \mathbf{T}_{\text{sca}}^j \left\{ \beta^{(j,0)} \begin{bmatrix} \mathbf{a} \\ \mathbf{b} \end{bmatrix} + \sum_{\substack{l=1 \\ l \neq j}}^{N} \alpha^{(j,l)} \begin{bmatrix} \mathbf{p}^j \\ \mathbf{q}^j \end{bmatrix} \right\}, \quad j = 1, \dots, N, \tag{10}$$

where $\beta^{(j,0)}$ and $\alpha^{(j,l)}$ represent the first and third kind vector translation-addition expansion coefficients, respectively [29, 30]. To simplify the notation, in what follows we use $\mathbf{T}^j$ instead of $\mathbf{T}_{\text{sca}}^j$. Then, by introducing the column vectors, $\mathbf{v}^j = \left[\mathbf{p}^j, \mathbf{q}^j\right]^T$, $j = 1, \dots, N$, $\mathbf{V} = \left[\mathbf{v}^1, \mathbf{v}^2, \dots, \mathbf{v}^N\right]^T$, $\mathbf{u} = [\mathbf{a}, \mathbf{b}]^T$, and $\mathbf{U} = \left[\mathbf{T}^1 \beta^{(1,0)} \mathbf{u}, \mathbf{T}^2 \beta^{(2,0)} \mathbf{u}, \dots, \mathbf{T}^N \beta^{(N,0)} \mathbf{u},\right]^T$, the solution of the scattering problem can be found by solving the following matrix equation:

$$\mathbf{S} \cdot \mathbf{V} = \mathbf{U}, \tag{11}$$

where the scattering matrix of the system is expressed as:

$$\mathbf{S} = \begin{pmatrix} \mathbf{I} & -\mathbf{T}^1 \alpha^{(1,2)} & -\mathbf{T}^1 \alpha^{(1,3)} & \cdots & -\mathbf{T}^1 \alpha^{(1,N)} \\ -\mathbf{T}^2 \alpha^{(2,1)} & \mathbf{I} & -\mathbf{T}^2 \alpha^{(2,3)} & \cdots & -\mathbf{T}^2 \alpha^{(2,N)} \\ -\mathbf{T}^3 \alpha^{(3,1)} & -\mathbf{T}^3 \alpha^{(3,2)} & \mathbf{I} & \cdots & -\mathbf{T}^3 \alpha^{(3,N)} \\ \vdots & \vdots & \vdots & \ddots & \vdots \\ -\mathbf{T}^N \alpha^{(N,1)} & -\mathbf{T}^N \alpha^{(N,2)} & -\mathbf{T}^N \alpha^{(N,3)} & \cdots & \mathbf{I} \end{pmatrix}. \tag{12}$$

The construction of the scattering matrix, $\mathbf{S}$, and finding the solution, $\mathbf{V}$, of the system (11) represent the main parts of the MSM method. Regarding these main steps, a couple of remarks are in order. Thus, in a practical numerical implementation of the MSM method, the field series expansions are truncated to a certain order of harmonics, n_{max}. The value of n_{max} depends on the particles size number, $x = ka$, and the maximum separation distance between any two particles in the scattering system. Therefore, the matrix defining this system is completely determined by the location, shape and materials parameters of the nanoparticles. Furthermore, the matrix $\mathbf{S}$ of the system has a block structure, where the diagonal blocks consist of single-particle T-matrices and the off-diagonal blocks are matrices that describe the inter-particle interaction. The unknowns of the scattering problem, grouped in the vector $\mathbf{V}$, can be used to compute physical quantities that characterize the wave scattering, namely, the electromagnetic field distribution inside and outside the scatterers, and the scattering, absorption, and extinction cross-sections.

4. Light scattering by a single and a chiral cluster of silicon nanospheres

In this section we investigate the scattering of PWs and LG beams from a single silicon nanosphere and chiral clusters made of such nanospheres, by using the numerical implementation of the MSM method outlined in Section 3. As a generic example of chiral clusters we consider an Archimedes-like spiral with q-fold rotational symmetry ($q = 3$ and $q = 4$ in our case). In our study we are particularly interested in the transfer of angular momentum from the incident PWs and LG beams to the scattered field and how the optical modes of the nanospheres and the symmetry properties of the cluster affect this transfer of angular momentum.

4.1. Light scattering by a single silicon nanosphere

We begin our analysis by considering the light scattering from a single silicon nanosphere, a physical set-up that can be described analytically, too. This provides us a reliable setting to validate our numerical implementation of the MSM method and the algorithm used to construct LG
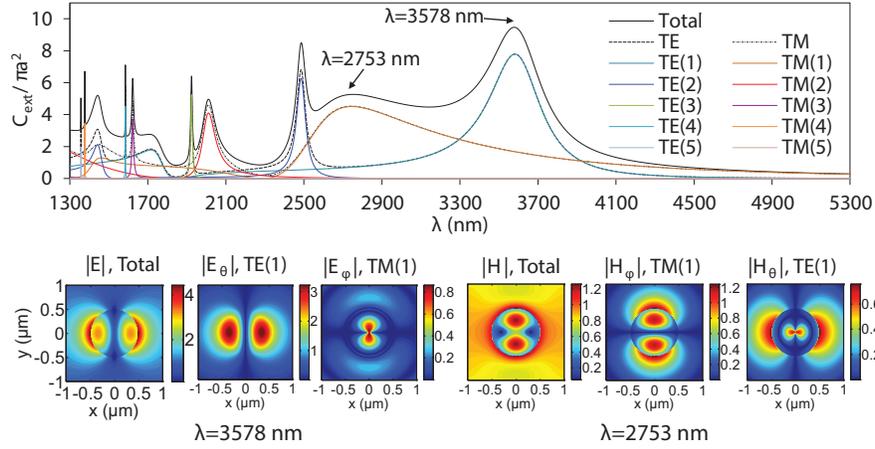
Fig. 3. Top panel shows the the spectra $C_{ext}(\lambda)$ calculated for a 500 nm silicon nanosphere, normalized to the cross-section area of the sphere. The excitation is a linearly polarized PW ($\sigma = 0$). The index in parentheses in the legend indicates the multipole order. In the bottom panel, the left (right) set of three plots represents, from left to right, the spatial distribution of the total electric (magnetic) field, the longitudinal component of the electric (magnetic) field of the first-order TE mode, TE(1), and the azimuthal component of the electric (magnetic) field of the first-order TM mode, TM(1).

beams. Thus, we considered a silicon nanosphere with radius, $a = 500$ nm, placed at the system origin and calculated the spectrum of the extinction cross-section, $C_{ext}(\lambda)$. We considered as incident excitation both a PW and LG beams, LG_{0l}, $l = 1, 2, 3, 4$, and in both cases the waves were LP ($\sigma = 0$), LCP ($\sigma = 1$), and RCP ($\sigma = -1$). In order to avoid the spectral regions where silicon has large optical linear absorption, we varied in our calculation the wavelength, λ, of the incident light from 1300 nm to 5300 nm.

In order to understand the structure of the scattered light, we show in the top panel of Fig. 3 the spectra of the decomposition of C_{ext}, in terms of transverse magnetic (TM) and transverse electric (TE) multipoles [40, 41]. In particular, we present the spectrum of the total C_{ext}, the spectra of C_{ext} for both the total TE and TM part of the scattered field, as well as the spectra of the first 5 TE and TM polarized modes. As Fig. 3 illustrates, the spectrum of C_{ext} contains a series of resonances, which become narrower and more closely spaced as the wavelength decreases. Moreover, it can be seen that at large wavelengths C_{ext} contains the contribution of only a few such modes (multipoles), whereas the smaller the wavelength becomes a larger number of modes must be included in order to achieve an accurate representation of C_{ext}.

The nature of the spectral resonances in Fig. 3 is further illustrated by the field profiles of the dominant TE and TM resonances, denoted in the legend of this figure by TE(1) and TM(1), respectively. These dipole resonances correspond to $\lambda = 3578$ nm (TE) and $\lambda = 2753$ nm (TM). These field profiles clearly demonstrate that at $\lambda = 3578$ nm the main contribution to the electric field comes from the TE(1) dipole electric mode, although the TM(1) dipole magnetic mode and higher-order multipoles are (weakly) excited at this wavelength, too. At $\lambda = 2753$ nm the reverse situation occurs, namely the dominant contribution to C_{ext} comes from the TM(1) mode, although the TE(1) and higher-order multipoles exist, too.

We now consider the light scattering by the same silicon nanosphere, but as incident optical wave we assume both PWs and LG beams, LG_{0l}, with $l = 1, 2, 3, 4$. In addition, in order to
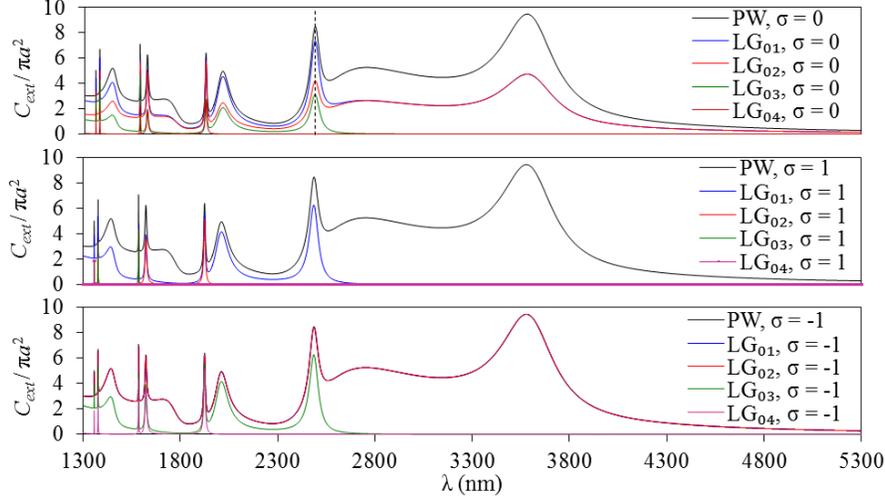
Fig. 4. Spectra of C_{ext} vs. wavelength, calculated for a silicon nanosphere with radius $a = 500$ nm. The incoming excitations are PWs and LG beams, LG_{0l}, $l = 1, 2, 3, 4$. From top to bottom, the panels correspond to the spin number $\sigma = 0$, $\sigma = 1$, and $\sigma = -1$. The vertical line corresponds to the wavelength of the TE(2) resonance, $\lambda = 2487$ nm.

understand how the scattering process is affected by the wave polarization, we assume that the incident beam carry a spin angular momentum characterized by the spin number $\sigma = 0, \pm 1$. Hence, the beams carry a total angular momentum characterized by the quantum number $j = l + \sigma$. Moreover, LG_{0l} beams with $\sigma = \pm 1$ contain only multipole modes with $n \geq l + \sigma$, so that we introduce the integer $n_{min}^+ = l + 1$ ($n_{min}^- = l - 1$) corresponding to $\sigma = 1$ ($\sigma = -1$), which defines the minimum multipole order of the incoming and scattered waves. The case of linearly polarized light, $\sigma = 0$, can be understood as the linear superposition of two modes with $\sigma = 1$ and $\sigma = -1$. With this notation, we have that for $l = 1, 2, 3, 4$ the minimum values of the mode numbers are $n_{min}^+ = 2, 3, 4, 5$ and $n_{min}^- = 1, 1, 2, 3$, respectively (remember that $n \geq 1$).

Figure 4 shows the spectrum of C_{ext} corresponding to the incident beams that we have just discussed. It illustrates a series of important phenomena regarding the dependence of the wave scattering process on the content of optical angular momentum of the incident beam. First, let us compare the plots in the top panel, which correspond to $\sigma = 0$. It can be seen that as l increases, the scattering channels that correspond to small values of the multipole order, n, are completely suppressed. For example, it can be seen that the light scattering in modes with $n = 1$ ($\lambda = 3578$ nm and $\lambda = 2753$ nm), namely the TE(1) and TM(1) resonances, vanishes if the incident beam is either one of the LG_{03} or LG_{04} beam. Indeed, these beams contain only multipoles with $n \geq 2$ and $n \geq 3$, respectively, so that the conservation of the projection of the total angular momentum along the beam axis implies that these beams cannot excite Mie dipole resonances corresponding to $n = 1$. This effect, called angular-momentum-induced transparency [27], can find useful applications to selective filtering of components of optical beams that carry specific values of angular momentum.

This same effect is observed when $\sigma = \pm 1$, too, the spectra of C_{ext} corresponding to these two cases being presented in the last two panels of Fig. 4. We can see that indeed when the incident wave is a LG_{0l} beam, the scattered field does not contain multipole modes with $n = 1$ if $l \geq 1$ for $\sigma = 1$ and $l \geq 3$ for $\sigma = -1$. Moreover, as l increases, multipole modes of higher order become completely suppressed. Figure 4 reveals another important feature of the extinction

cross-section, namely that there are pairs of the numbers l and σ for which C_{ext} is the same. For example, C_{ext} for $l = 3$ and $\sigma = -1$ is identical with C_{ext} for $l = 1$ and $\sigma = 1$, a result explained by the fact that in both cases $n_{min} = 2$ and therefore the scatterred field contains the same set of Mie coefficients. In addition, we note that C_{ext} for an incident beam, LG_{01} with $\sigma = 1$ ($n_{min}^+ = 1$), an incident beam, LG_{02} with $\sigma = -1$ ($n_{min}^+ = 2 - 1 = 1$), and an incident PW have almost identical values. This is due to the fact that in our calculations the beam waist, $w_0 = \lambda$, and thus in the spectral range considered in our computations, $1300 \, \text{nm} \leq \lambda \leq 5300 \, \text{nm}$ one has $w_0 \gg a$. In other words, across the nanosphere the field profile of the LG beams is similar to that of a PW.

4.2. Light scattering by a chiral cluster of silicon nanospheres

We now consider scatterers with a more complex structure, namely we study the scattering of PWs and LG beams, LG_{01}, $l = 4, 5$, from chiral structures consisting of silicon nanospheres arranged in an Archimedes-like spiral with q-fold rotational symmetry; specifically, $q = 3$ and $q = 4$ in our calculations. Under these conditions the continuous rotational symmetry of the scatterer is broken so that if the incident light has well-defined optical angular momentum it can scatter only in a set of modes with specific values of the total optical angular momentum.

In order to illustrate these ideas we present in Fig. 5 the extinction cross-section, C_{ext}, calculated for the two chiral clusters we just described. The calculations for the chiral cluster with $q = 3$ are performed for a linearly polarized PW ($\sigma = 0$) and a LG_{04} beam with $\sigma = \pm 1$, whereas for the chiral cluster with $q = 4$ we calculated C_{ext} for a linearly polarized PW and a LG_{05} beam with $\sigma = \pm 1$. In both cases we plot C_{ext}, normalized to the total transverse area of the nanospheres in the cluster, corresponding to the TE and TM decomposition of multipoles, the spectra of the normalized C_{ext} corresponding to TE(1), TE(2), TM(1), and TM(2), as well as the spectrum of the total, normalized C_{ext}. In all these calculations we included $n_{max} = 15$ orders in the Mie expansion of the electromagnetic fields, which was enough to achieve convergence in the entire spectral domain, $1300 \, \text{nm} \leq \lambda \leq 5300 \, \text{nm}$.
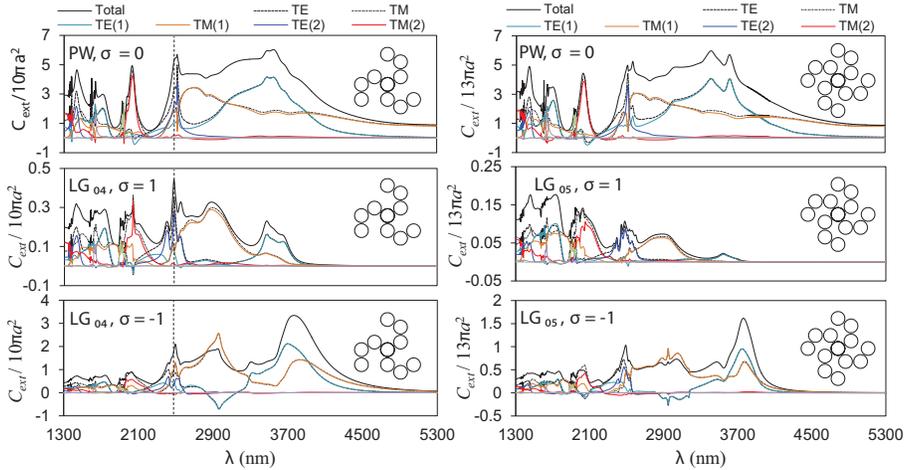

Fig. 5. Spectrum of normalized C_{ext} corresponding to chiral structures with q-fold symmetry made of silicon nanospheres with radius, $a = 500 \, \text{nm}$. Left panels correspond to $q = 3$, incident PW with $\sigma = 0$, and LG_{04} beams with $\sigma = \pm 1$, whereas right panels correspond to $q = 4$, incident PW with $\sigma = 0$, and LG_{05} beams with $\sigma = \pm 1$. The vertical line corresponds to the wavelength of the TE(2) resonance, $\lambda = 2515 \, \text{nm}$.
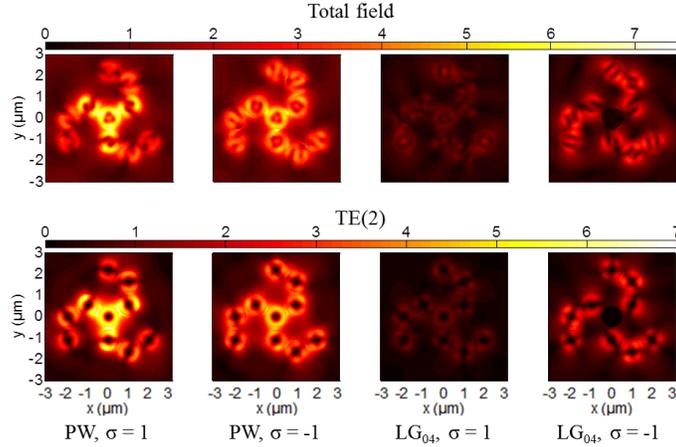
Fig. 6. Spatial distribution of the magnitude of the electric field calculated at $\lambda = 2515\,\text{nm}$. From left to right column, the panels correspond to a PW with $\sigma = 1$, a PW with $\sigma = -1$, a LG$_{04}$ with $\sigma = 1$, and a LG$_{04}$ with $\sigma = -1$. The top and botom panels correspond to the total field and the field corresponding to the TE(2) quadrupole mode, respectively.

The influence of the discrete nature of the rotation symmetry group of the cluster is clearly illustrated in Fig. 5. Thus, if the total optical angular momentum of the incident beam is characterized by the integer $j_{inc} = l + \sigma$, and if the cluster has q-fold rotational symmetry, the scattered field will contain modes with total optical angular momentum, $j_{sca} = j_{inc} + \nu q = l + \sigma + \nu q$ [36], where ν is an integer. In other words, the cluster compensates for the difference between the total optical angular momentum of the incident and scattered fields the same way a diffraction grating can compensate for the difference between the wavevectors of two interacting optical waves. More specifically, let us consider first the cluster with $q = 3$ and incident beam, LG$_{04}$, with $\sigma = 1$. Then, the quantum number characterizing the total optical angular momentum of the modes of the scattered field is $j_{sca} = 5, 5 \pm 3, 5 \pm 6, \ldots$. Since the larger the integer ν the weaker the scattering process is, we expect that the dominant multipole modes will have $j_{sca} = 5 - 3 = 2$, corresponding to $\nu = -1$, namely the TE(2) and TM(2) quadrupole modes. Note, however, that the TE(1) and TM(1) modes can be excited, too, a case that corresponds to $\nu = -2$. This conclusion is indeed supported by the plots in Fig. 5 (see the blue and red lines). If, on the other hand, one reverses the spin of the LG$_{04}$ beam, namely $\sigma = 1 \rightarrow \sigma = -1$, the C_{ext} of the TE(2) and TM(2) modes is significantly reduced as in this case $j_{sca} = 3, 3 \pm 3, 3 \pm 6, \ldots$. Note also that C_{ext} is much smaller when $\sigma = 1$ as compared to the $\sigma = -1$ case. The reason is that the cluster itself is chiral and therefore the light-cluster coupling strength depends on σ. Similar conclusions, supported by the plots in Fig. 5, can be derived for the cluster with $q = 4$.

We stress that the cluster of nanospheres does not have to be a chiral structure for the conclusions derived above to be true. Moreover, the transfer of optical angular momentum from the incident to the scattered field would occur even if the cluster would have contained uniform, structureless branches. If the cluster is made, however, from resonators, this transfer of optical angular momentum is resonantly enhanced. This conclusion is supported by the fact that enhanced orbital angular momentum conversion is observed at the wavelengths of the TE(2) and TM(2) resonances *of the cluster*, whose values are very close to those of the TE(2) and TM(2) resonances, respectively, *of the nanospheres*. For example, the wavelengths of the TE(2) resonance of the cluster and nanospheres are $\lambda = 2515\,\text{nm}$ and $\lambda = 2487\,\text{nm}$, respectively, the difference being due to the optical coupling of the nanospheres in the cluster.

If the cluster is chiral, unsurprisingly, additional differences in the physical properties of the scattered field can be observed when the spin of the incident beam is reversed. This is valid not only for LG beams but even in the case when a circularly-polarized PW impinges onto the chiral cluster. This behavior is illustrated by the spatial distribution of the near-field plotted in Fig. 6. Thus, we consider the chiral cluster with 3-fold symmetry and assume that the incident wave is a PW with $\sigma = 1$, a PW with $\sigma = -1$, a LG$_{04}$ with $\sigma = 1$, and a LG$_{04}$ with $\sigma = -1$. In all cases $\lambda = 2515$ nm, namely the wavelength corresponding to the TE(2) resonance. The plots in Fig. 6 show that indeed at this wavelength the total field is predominantly due to the resonant excitation of this quadrupole mode. In addition, a significant difference between the profiles of the near-fields corresponding to $\sigma = 1$ and $\sigma = -1$ can be clearly observed, too. In the case of PW excitation, the near-field has large value at the location of the central nanosphere, as the wavelength of the incident PW is close to the wavelength of the TE(2) quadrupole resonance of a single nanosphere (see Fig. 4). However, since the electromagnetic environment of this central nanosphere is chiral, the near-field distribution depends on the spin of the incident PW. These ideas are further discussed in the next section.

5. Generation of superchiral light

It has been recently demonstrated that chiral plasmonic nanostructures can be used to generate superchiral light [42–44], namely light for which, locally, the so-called chirality parameter is larger than that of circularly-polarized PWs. In this section we show that for this purpose all-dielectric structures are as efficient as plasmonic ones, the advantage provided by these structures being that chiral all-dielectric (silicon) nanostructures have significantly smaller losses.

To quantify the chirality of the optical near-field we use the chirality parameter, $\mathscr{C}(\mathbf{r})$, defined as [42]:

$$\mathscr{C}(\mathbf{r}) = -\frac{\varepsilon\omega}{2}\mathrm{Im}\left[\mathbf{E}^*(\mathbf{r}) \cdot \mathbf{B}(\mathbf{r})\right]. \tag{13}$$
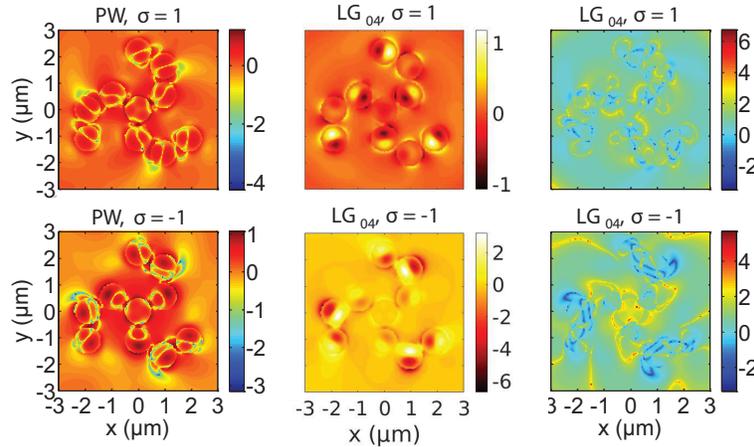

Fig. 7. Maps of the spatial distribution of the enhancement of the optical chirality, $\hat{\mathscr{C}}(\mathbf{r})$, calculated at $\lambda = 2515$ nm for PWs and LG$_{04}$ beams with $\sigma = \pm1$, incident on a chiral cluster of silicon nanoparticles with radius, $a = 500$ nm, with 3-fold rotational symmetry. In the left (logarithmic plots) and middle panels the optical chirality is normalized to the optical chirality of a circularly-polarized PW, whereas in the right panel (logarithmic plots) the optical chirality is normalized to the *local* optical chirality corresponding to an incident circularly-polarized PW with the same value of σ.

Using this definition, one can calculate the local enhancement of the optical chirality:

$$\hat{\mathscr{C}}(\mathbf{r}) = \frac{\mathscr{C}^{tot}_{\{PW^\pm, LG^\pm\}}(\mathbf{r})}{\left| \mathscr{C}^{\{tot,inc\}}_{PW^\pm}(\mathbf{r}) \right|}. \tag{14}$$

Here the superscripts $\{tot, inc\}$ refer to $\mathscr{C}(\mathbf{r})$ being computed from the total or the incident electromagnetic fields, respectively, whereas the subscripts $PW^\pm$ and $LG^\pm$ refer to PWs and LG beams with $\sigma = \pm 1$, respectively. Since circularly-polarized PWs have $|\mathscr{C}| = 1$, the regions with superchiral light are defined by the relation, $|\mathscr{C}(\mathbf{r})| > 1$.

   Figure 7 shows the spatial distribution of the local optical chirality enhancement calculated using Eq. (14), at the resonance wavelength $\lambda = 2515\,\mathrm{nm}$ of the TE(2) quadrupole mode. We have considered as incident wave both PWs and LG_{04} beams and in both cases the beams were assumed to be circularly polarized with $\sigma = \pm 1$. In the case of PW excitation the local optical chirality was normalized to the optical chirality of a circularly-polarized PW. In the case of LG beams, whose optical chirality is position dependent, the local optical chirality was normalized to the optical chirality of a circularly-polarized PW as well as to the *local* optical chirality corresponding to an incident circularly-polarized PW with the same value of σ as that of the LG_{04} beam. These calculations demonstrate that all-dielectric chiral nanostructures can be used effectively to achieve large enhancement of the optical chirality, by more than one order of magnitude, that is an enhancement comparable to that achievable in plasmonic structures. This can be realized, however, without employing plasmonic effects; that is, achieving large local field enhancements is not a prerequisite for the generation of superchiral light.

6.   Conclusion

To summarize, we have demonstrated that nanophotonic structures made of all-dielectric resonators can be efficiently employed in creating optical fields with specific characteristics of their optical angular momentum. In particular, our theoretical analysis has revealed that by using silicon nanospheres arranged in clusters that are invariant to specific rotation transformations one can resonantly enhance or suppress the transfer of optical angular momentum from incident plane waves or more complex optical beams, such as Laguerre-Gaussian beams, to scattered fields with specific values of the orbital and spin angular momentum. We have shown that this angular momentum transfer can be strongly affected by the resonant excitation of optical modes of the resonators forming the cluster, as well as by the specific mixture of orbital and spin angular momentum carried by the excitation optical beam.

   As a practical application of these ideas, we have demonstrated that chiral clusters made of silicon nanospheres can be effectively used to generate superchiral optical near-fields whose optical chirality can be more than an order of magnitude larger than that of plane waves. This functionality can be achieved without having to pay the price of large optical losses, which is largely unavoidable if plasmonic systems are used. Since the more superchiral light is the stronger it interacts with chiral molecules, our work can find important applications to near-field optical microscopy, surface science, and sensing. Equally important, by arranging the clusters investigated in this study in two-dimensional arrays, one can create all-dielectric metasurfaces that can be used to generate optical beams with new, pre-designed functionalities.